Materials Today Communications 52 (2026) 115100

Contents lists available at ScienceDirect

Materials Today Communications

journal homepage: www.elsevier.com/locate/mtcomm

Size dependence of lattice strain anisotropy in nickel and ceria under non-hydrostatic compression

Mingzhi Yuan [a,b], Jianing Xu [a,b], Haini Dong [b], Xiaoling Zhou [a,*], Bin Chen [a,b,c,**]

[a] School of Science, Harbin Institute of Technology, Shenzhen 518055, PR China
[b] Center for High Pressure Science and Technology Advanced Research, Shanghai 201203, PR China
[c] Institute for Shanghai Advanced Research in Physical Sciences, Shanghai 201203, PR China

ARTICLE INFO

Keywords:
Non-hydrostatic high pressure
Lattice strain
Nanomaterials
Elastic-plastic deformation
Nickel
Ceria

ABSTRACT

Strain engineering under extreme non-hydrostatic compression provides a unique pathway to tune material properties, yet the evolution of fine structural parameters under such conditions remains unexplored. Here, we systematically investigate the elastic-plastic deformation behaviors of nickel and ceria (CeO_2) across varying grain sizes (8–200 nm) under non-hydrostatic compression up to ~35 GPa using synchrotron-based radial X-ray diffraction in a diamond anvil cell. We find that the differential lattice aspect ratio in nickel plateaus at a relatively low pressure due to yielding, whereas ceria exhibits continuous elastic deformation with an increasing aspect ratio within the tested pressure range. Furthermore, as the grain size decreases to ~8 nm, the maximum differential lattice aspect ratios of {200} plane in both nickel and ceria reach ~3.2%. The lattice strain anisotropy experiences a multifold enhancement in nickel as the grain size reduces from ~200 nm to ~8 nm due to the suppression of dislocation slip. In contrast, this increase of anisotropy by reduction of grain size attenuates in ceria, a phenomenon attributed to the activation of nanoscale plasticity in nanoceramics. These size-dependent deformation mechanisms are further corroborated by microstructural evidence from transmission electron microscopy. Our results highlight the broad tunable parameter space in both metallic- and covalent-bonded nanomaterials via non-hydrostatic high-pressure strain engineering, and would help to understand the high-pressure strengthening effect in nanograined metals.

1. Introduction

Strain engineering is a highly promising strategy that has propelled research in condensed matter physics and materials science by altering the fundamental structural parameters of materials. Through strain engineering, unprecedented phenomena and properties have been discovered across diverse systems including two-dimensional materials, diamond, perovskites, electrocatalysts and nanometals [1–6]. Compared to conventional approaches of strain engineering such as uniaxial tension, pure shear, or chemically induced strain whose tunable ranges are inherently limited by fracture, plasticity, or specific chemical properties, high-pressure techniques allow us to explore a vast regime of negative stress, potentially extending to the theoretical ideal strength limit of materials [7–9]. To date, this area has been mostly constrained to quasi-hydrostatic conditions without significant shear stress. However, the parameter space can be substantially broadened through the fundamental understanding and exploitation of non-hydrostatic compression. With the development of synchrotron-based radial X-ray diffraction (RXRD) measurements in diamond anvil cells (DACs) without pressure transmitting media, it is now possible to experimentally detect the deformation behavior and yield strength of materials under extreme non-hydrostatic stress states [10–13], which is crucial for the guidance of strain engineering under such conditions.

Nanocrystalline materials often exhibit enhanced mechanical properties owing to their large surface-area-to-volume ratios [13–16]. For instance, in nanograined metals, the suppression of dislocation slip by a high density of grain boundaries leads to the well-known Hall-Petch effect [17,18], where smaller grain sizes correspond to higher yield strengths. Similarly, in ZnS nanoparticles, competing relaxation from irregular surfaces causes inhomogeneous internal strain, contributing to structural stiffening [16]. These characteristics theoretically grant nanomaterials unique advantages for elastic strain engineering. Because

* Corresponding author.
** Corresponding author at: School of Science, Harbin Institute of Technology, Shenzhen 518055, PR China.
E-mail addresses: zhouxiaoling@hit.edu.cn (X. Zhou), chenbin@hpstar.ac.cn (B. Chen).

https://doi.org/10.1016/j.mtcomm.2026.115100
Received 21 January 2026; Received in revised form 8 March 2026; Accepted 30 March 2026
Available online 30 March 2026

they can withstand substantially higher stress levels without inelastic relaxation, they afford a vastly broadened parameter space for the optimization of functional properties [7]. Nevertheless, the exact extent to which this parameter space can be expanded remains elusive. Therefore, it is of great value to investigate the elastic-plastic deformation behavior of nanocrystalline materials and extract fine structural information, particularly under non-hydrostatic high-pressure conditions.

In the present study, nickel and ceria (CeO_2) are selected as representative model systems for metallic and ceramic classes, respectively, to systematically investigate the influence of crystallite size (down to the tens of nanometers) on their deformation behaviors under non-hydrostatic compression. By analyzing the RXRD data obtained in a DAC, we estimate the strain differential between lattice planes oriented parallel and perpendicular to the principal stress axis, and track its evolution with increasing pressure in each sample. We find that this strain differential, which reflects the intrinsic mechanical response of the material, is strongly size-dependent and fundamentally distinct between metals and ceramics. With the support from transmission electron microscopy (TEM) characterization, we attribute this behavior to differences in the propensity for plastic deformation between metallic- and covalent-bonded materials across different grain sizes. The implications of our findings regarding general high-pressure strain engineering and the underlying strengthening mechanism of nanograined metals are discussed.

2. Experiment and analysis methods

To elucidate the impact of nanomaterials' grain size on the deformation behavior, samples with 3–4 different sizes from the deep nanoscale regime to the ultrafine-grained regime were investigated in both nickel and ceria. For nickel, powders with average grain sizes of ~8 nm, ~20 nm, ~75 nm and ~200 nm were selected. For CeO_2, powders with average grain sizes of ~8 nm, ~40 nm and ~200 nm were selected. The characterization of the original samples can be found in the supplementary material.

High-pressure loading was achieved using a panoramic DAC equipped with 300 μm culet anvils. X-ray transparent gaskets (made of compacted amorphous boron-epoxy mixtures) for RXRD were secured on the top of the anvil by Kapton wafers. The diameter of the laser-milled sample chamber in the gaskets was approximately 60 μm. In each experimental run, sample powders were loaded into the chamber alongside a small piece of Pt foil (~10 μm) serving as the pressure calibrant [19]. Crucially, the introduction of a pressure-transmitting medium was intentionally omitted to geometrically maximize the macroscopic shear stress generated by the anvils. In-situ X-ray diffraction (XRD) measurements in a radial geometry during compression (Fig. 1a) were conducted at beamline 12.2.2, Advanced Light Source, Lawrence Berkeley National Laboratory. The incident X-ray energy was 25 keV, and diffraction patterns were collected using a mar345 Image Plate Detector. Instrumental parameters were calibrated with CeO_2 and LaB_6 standards for the nickel and CeO_2 runs, respectively. The obtained data were processed using FIT2D [20] and Multifit [21] for analysis.

For TEM observation, lamellae thinner than 100 nm were extracted using a Zeiss Auriga focused ion beam (FIB) system from the recovered samples which had been compressed separately in steel gaskets. To prevent possible artifacts, a protective Pt layer was deposited onto the target surface of each sample prior to ion milling. Characterization was performed using an aberration-corrected transmission electron microscope (Titan G2 60–300) operating at 300 kV in scanning transmission electron microscopy (STEM) mode.

To better illustrate the principle of estimating lattice strain anisotropy in our work, we briefly describe the setup of DAC-RXRD experiments and our analytical methodology. As depicted in Fig. 1a, the incident X-ray beam penetrates the gasket and produces a diffraction pattern from the sample on the detector located on the opposite side. Unlike conventional DAC-XRD experiments in which the beam traverses the diamond anvils and interacts only with crystallographic planes symmetrically oriented to the compression axis, this geometry enables the detection of planes at various angles relative to the uniaxial compression direction. The azimuth angle ψ is determined by the projection of the compression axis and the diffraction vector on the detector.

Based on the geometric relationships of the RXRD, we can extract lattice strain information from monocrystalline grains possessing specific orientations within the powder samples. Here we discuss a simplified scenario. As shown in Fig. 1b, the red plane that satisfies the diffraction condition at 2θ and has a normal vector closely aligned with the compression axis will generate a diffraction signal at $\psi \approx 0°$. Rotating around this normal vector yields all crystals containing this specific plane, including instances where another equivalent plane from the same monocrystalline grain also satisfies the diffraction condition. Given the inherent cubic symmetry of the crystallographic systems under investigation, the orthogonal equivalent set of planes inevitably generates a diffraction signal at $\psi \approx 90°$ or 270°, as illustrated in Fig. 1c (the green plane, showing the $\psi \approx 90°$ case). Due to differential stress, this signal occurs at a slightly different diffraction angle, $2\theta'$. Therefore, the anisotropic lattice strain within the materials can be calculated using 2θ and $2\theta'$ measured in our experiments. In other words, for cubic systems, pairs of powder diffraction peaks separated by a 90° azimuthal offset can originate from orthogonal equivalent planes within a single monocrystalline grain. If the diffraction peaks shift in 2θ while remain symmetric, the lattice strain of the grain can be derived from the mean strain of the powder sample at these azimuth angles.

It should be noted that in actual diffraction geometries, an angle (θ) exists between the incident beam and the red plane, so its normal vector deviates slightly from the true vertically upward direction, and the signal from the corresponding green plane should locate at a ψ slightly

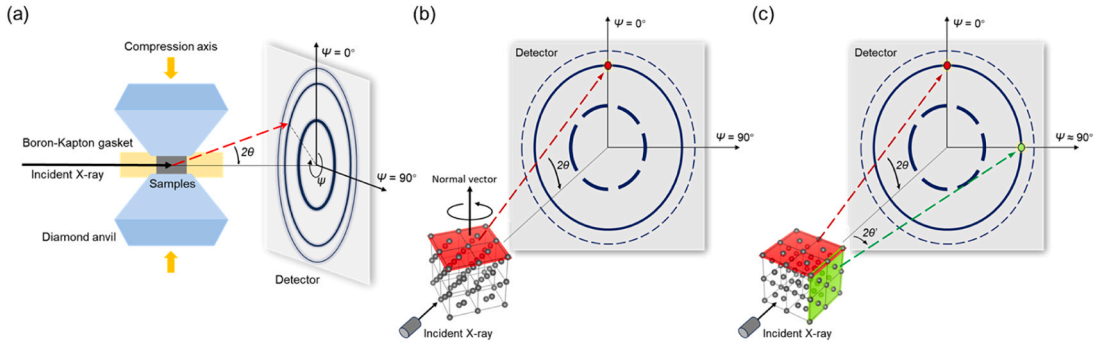

Fig. 1. (a) Schematic of the experimental setup for RXRD measurement in a DAC. (b–c) Visualized models illustrating the extraction of the lattice strain in the crystal with certain orientation from the RXRD data.

larger than 90°. In the following section, we will show that the θ we are analyzing is relatively small, making the increase in ψ negligible, thus reasonable approximation could be applied when estimating the anisotropic lattice strain.

3. Results and discussion

We first demonstrate the result from 8 nm nickel in detail as an example of the real case analysis. Fig. 2a shows the diffraction pattern collected at the maximum pressure of the run (~39.4 GPa). As a result of the non-hydrostatic stress tensor, the Debye-Scherrer rings exhibit elliptical distortion, with the major axis aligns parallel to the principal compressional stress vector. The red and green arrows in Fig. 2a indicate shifts toward higher and lower diffraction angles for planes subjected to differential stress (compared to the planes under hydrostatic compression at equivalent pressures), respectively. In Fig. 2b, the distortion of the rings is accentuated by the curvature of the azimuthally unrolled pattern.

For cubic materials like nickel and ceria, we focus on the {200} reflections because they directly determine the unit cell parameter a and exhibit minimal sensitivity to plastic deformation effects. At each pressure point, the unrolled patterns were evenly divided into 72 segments at 5° intervals, and the d-spacing of {200} plane was determined by peak fitting within each segment. The good symmetry of the peaks across different azimuth angles further supports the validity of our approach for estimating lattice strain in monocrystalline grains from powder diffraction data (Fig. 2c). Fig. 2d shows the d-spacing against the azimuth angle at selected pressures. As the figure indicates, the curvature of the calculated d-spacing pattern increases rapidly at relatively low pressures, however, at pressures exceeding ~6.7 GPa, the pattern shifts entirely toward smaller d-spacings with minimal changes in curvature. This behavior contrasts with findings from a similar X-ray diffraction study on stressed nanopolycrystalline diamond, wherein the pattern curvature increased but did not integrally shift with stress and became saturated at certain level [22]. We attribute this discrepancy to the enormous strength difference between our samples and the nanopolycrystalline diamond, as well as the distinct stress states induced by varying loading techniques.

The d-spacing patterns could be fitted using the equation

$$d_m(200) = d_p(200)\{1 + [1 - 3\cos^2(\psi + \alpha)]Q(200)\} \quad (1)$$

Here, d_m represents the measured d-spacing, d_p is the spacing under hydrostatic pressure (obtained at the "magic angle" where $\psi+\alpha$=54.7°), α is a corrective angle accounting for the misalignment between the compression axis and the vertical axis of the detector, and Q denotes the azimuthal oscillation induced by differential stress [10,22]. From this fit, we derive the d-spacing with the minimum and maximum compressional strain, d_{max} and d_{min}, and estimate the lattice strain anisotropy in certain monocrystalline grains as discussed in the previous section. The difference between d_{max} and d_{min} indicates how the cubic unit cells are "squashed" by the non-hydrostatic compression, as schematically depicted in Fig. 2e.

To track the evolution of this lattice strain anisotropy across varying pressures and samples, we analysed the {200} planes for all the nickel and ceria samples (Fig. S8, supplementary materials). We define the differential lattice aspect ratio $r = (d_{max} - d_{min})/d_{max} \times 100\%$, referring the difference between the lattice planes with maximum and minimum d-spacing in percentage, to quantify the anisotropy of the lattice strain. Fig. 3 plots r as a function of pressure in Ni and CeO_2 with different grain sizes. First, we compare the behavior of ultrafine-grained (200 nm) Ni and CeO_2. As the pressure elevates, the differential lattice aspect ratio in 200 nm Ni initially increases and then immediately reaches a plateau with a relatively low value below 0.8% (Fig. 3a). In contrast, the ratio in 200 nm CeO_2 increases continuously with the pressure, ultimately exceeding 2% at the maximum applied pressure (Fig. 3b). This could be interpreted by the different deformation mechanisms in metals and ceramics. In the 200 nm Ni, the lattice initially deforms anisotropically under uniaxial compression; however, at a critical pressure (~1.9 GPa), the material yields, and plastic slip becomes the dominant deformation mechanism. This causes the lattice to contract with a constant r during subsequent compression, with any further increases in differential stress stemming solely from the pressure-induced increase in the shear modulus. Conversely, in the 200 nm CeO_2, the absence of plastic slip forces the lattice to accommodate the differential stress through continuous anisotropic deformation, leading to an almost linear growth of r. This reveals intrinsic difference in the deformation behaviors of metallic- and covalent-bonded materials, highlighting the limit of the strain engineering range in ultrafine-grained metals compared to the

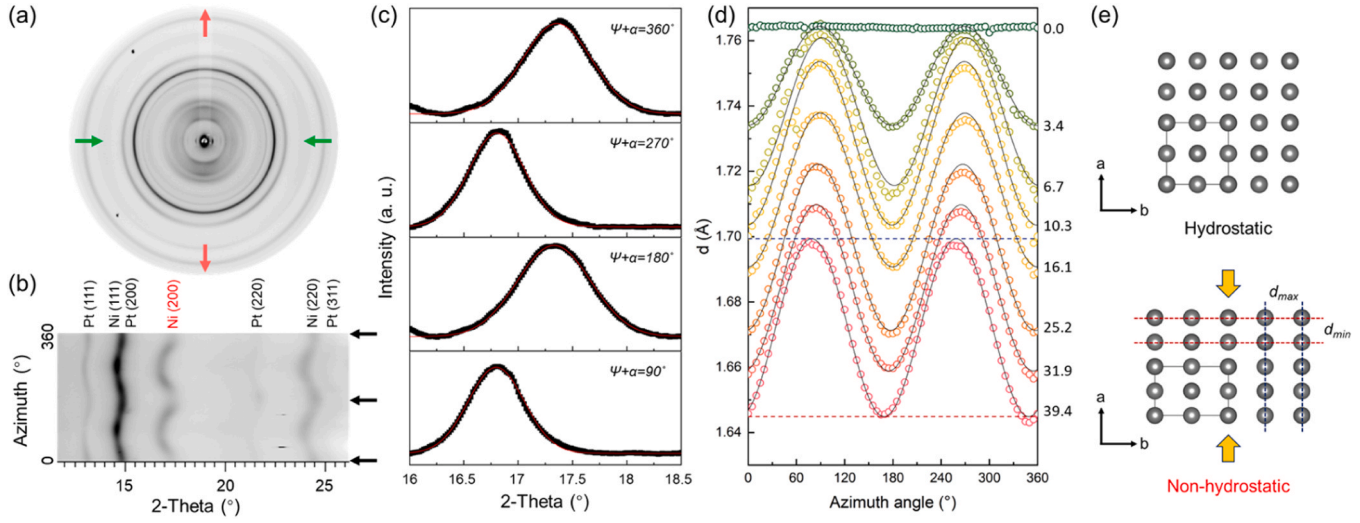

Fig. 2. (a) The collected Debye-Scherrer diffraction rings of 8 nm Ni and the pressure calibrant at ~39.4 GPa. The red and green arrows show the relative distortion of the rings compared with perfect circles. (b) Azimuthally unrolled diffraction data of (a). The black arrows point out the direction of the uniaxial compression. (c) Integrated diffraction peaks of Ni(200) at ψ+ α= 90°, 180°, 270° and 360° at ~39.4 GPa. The red solid lines are Gaussian fit of the peaks. (d) $d_{(200)}$ versus the azimuth angle at selected pressures (on the right, in GPa) of the 8 nm Ni. The black solid lines are the fitting results using (1), and the blue and red dashed lines are the calculated d_{max} and d_{min} at ~39.4 GPa, respectively. (e) Schematic of the unit cells being "squashed" by non-hydrostatic compression. The deformation is exaggerated for better illustration.

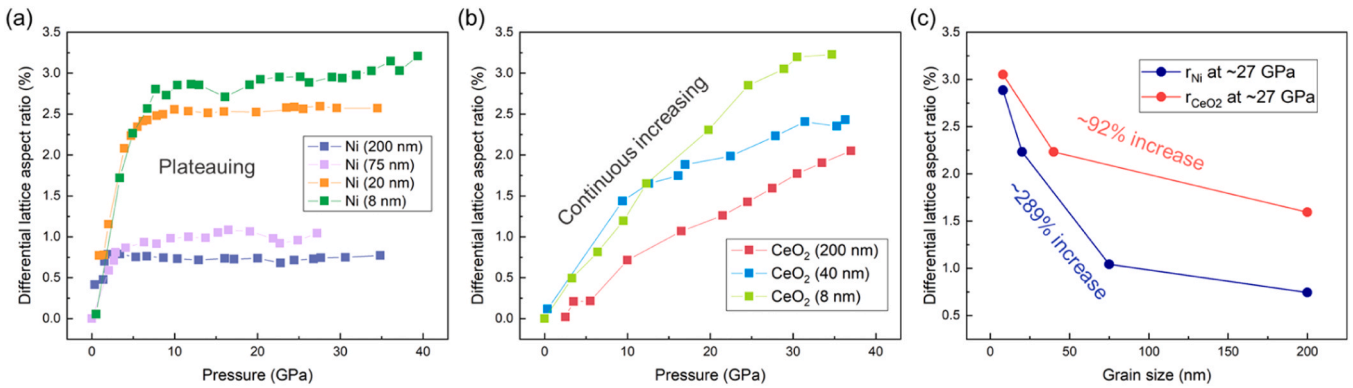

Fig. 3. (a) Differential lattice aspect ratio of Ni(200) in ultrafine-grained (200 nm) and nanograined (75 nm, 20 nm and 8 nm) Ni under non-hydrostatic high pressures. (b) Differential lattice aspect ratio of CeO_2(200) in ultrafine-grained (200 nm) and nanograined (40 nm and 8 nm) CeO_2 under non-hydrostatic high pressures. (c) The increases of differential lattice aspect ratios of Ni(200) and CeO_2(200) at ~27 GPa with decreasing grain sizes.

broader potential in compressed ultrafine-grained ceramics.

The nanograined samples exhibit distinct behavior in the lattice strain anisotropy under non-hydrostatic compression. As shown in Fig. 3a, *r* in 75 nm Ni increases linearly up to ~2.9 GPa and reaches a plateau at ~1.0%. For the 20 nm Ni, *r* keeps the linear increase to ~3.9 GPa before plateauing at ~2.5%. For the 8 nm Ni, a rapid growth stage persists until ~6.7 GPa, eventually reaching a maximum *r* (~3.2%) at ~39.4 GPa. The overall differential lattice aspect ratio in Ni has a pronounced size effect: smaller grain sizes correlate with higher achievable *r* values and require higher stress to reach saturation. Being similar to nanograined Ni, the nanograined CeO_2 samples also have larger *r* values compare to their ultrafine-grained counterpart, especially in the higher-pressure range (Fig. 3b). However, the relative increase in *r* achieved by reducing the grain size is markedly less significant in CeO_2 than in the Ni. The maximum *r* in 200 nm, 40 nm and 8 nm CeO_2 in the tested pressure range are ~2.1%, ~2.4% and ~3.2%, respectively. In Fig. 3c, we plot *r* against grain sizes at ~27 GPa to illustrate the different increase in the degree of lattice strain anisotropy in the two systems. The *r* in 8 nm CeO_2 (~3.0%) is only ~92% higher than in 200 nm CeO_2 at comparable pressure, in stark contrast to the multifold enhancement (~289% higher) observed in Ni.

The observed size-dependent differential lattice aspect ratio in both Ni and CeO_2 can be understood through their plastic behaviors. In metals, reducing the grain size to the nanometer-scale generally suppresses plastic slip due to the increased volume fraction of grain boundaries [23], enabling the material to sustain higher shear stress through elastic lattice deformation. This results in the higher upper limit of *r* in smaller-sized sample. Moreover, the different anisotropic lattice strain could have impact on the macroscopic stress–strain behavior, potentially explaining the reported deviation from the 0.2% offset criterion to define yielding in nanocrystalline metals [24]. In ceramics, size-induced bond stiffening causes the elevated *r* (higher differential stress) in smaller samples in the high-pressure regime. Crucially, the extreme localized stresses within these nanograins anomalously activate previously dormant plastic slip systems [25,26]. This stress-induced onset of nanoscale plasticity initiates localized yielding, which fundamentally accounts for the observed attenuation in the growth rate of *r*. The dramatic three-to-fourfold increase in lattice strain anisotropy of nanograined Ni compared to its ultrafine-grained counterpart suggests a vast tunable space for non-hydrostatic compression strain engineering. Conversely, this space in nanograined CeO_2, although comparable in magnitude to that of Ni, is less expanded by size reduction due to the onset of plastic deformation, especially considering the already relative high *r* value in ultrafine-grained CeO_2.

To further elucidate the plastic deformation within our samples, TEM characterizations were conducted on the samples recovered from the non-hydrostatic compressions. High-resolution transmission electron microscopy (HRTEM) images (Fig. 4a–d) reveal representative microstructures of defects in ultrafine-grain Ni, nanograined Ni, and nanograined CeO_2. In ultrafine-grained Ni (Fig. 4a), full dislocations are frequently observed. These dislocations could be attributed to the $\{111\}<1\bar{1}0>$ slip system, which is the predominant slip system in face-centered cubic metals [27]. In nanograined Ni, apart from full dislocations (Fig. 4b), deformation twins are also present as a consequence of plastic deformation (Fig. 4c). This is consistent with previous works reporting a transition from full dislocation slip to twinning as the primary plastic deformation mechanism in nanometals [13,28]. There should be other deformation mechanisms such as lattice rotation and grain boundary-assisted plasticity in the nanograined Ni [29–32], which could be further detected by *in-situ* characterization. Notably, full dislocations were also found in the compressed nanograined CeO_2 (Fig. 4d). This confirms our hypothesis regarding the less increased differential lattice aspect ratio in the material. The HRTEM images reveal the typical plastic deformation mechanisms active in nanograined Ni and CeO_2, refining our understanding of their lattice strain anisotropy under non-hydrostatic compression.

Our work provides a pathway to quantify the anisotropic lattice strain across different material classes under high pressures, offering critical insights for interpreting the frequently discussed structural transition, metallization and even superconductivity induced by non-hydrostatic compression [33–35]. Furthermore, the results suggest that substantial lattice strain anisotropy (up to ~3.2%) could be achieved in nanograined metals and ceramics through non-hydrostatic high-pressure strain engineering. This supports the anticipation that such strategies offer a much broader tunable space than conventional strain engineering methods, which typically achieve anisotropic strains below 1%. With the cognition established here, more ambitious and precise manipulations of the physicochemical properties via strain engineering can be expected.

Beyond illuminating the fine structural parameters of materials during strain engineering, the size-dependent lattice strain anisotropy holds implications for understanding the mechanical properties of nanograined metals. In the case of nanograined Ni under uniaxial compression, due to the suppression of dislocation slip by the concentrated boundaries and interfaces, the originally cubic unit cells will be "squashed" into cuboid cells when their c axes point close to the compression axis (Fig. 4e). This geometrical distortion can reduce the Schmid factor ($cos\varphi cos\lambda$, where φ and λ are the angles between the loading axis and the slip plane's normal vector and slip direction, respectively) of the slip systems, rendering them less active. The diminished slip activity leads to greater strain anisotropy, further reducing the Schmid factor. Specifically, in the 8 nm Ni subjected to non-hydrostatic compression, the actual Schmid factor of the $\{111\}<1\bar{1}0>$ slip system in the aforementioned unit cells decreases

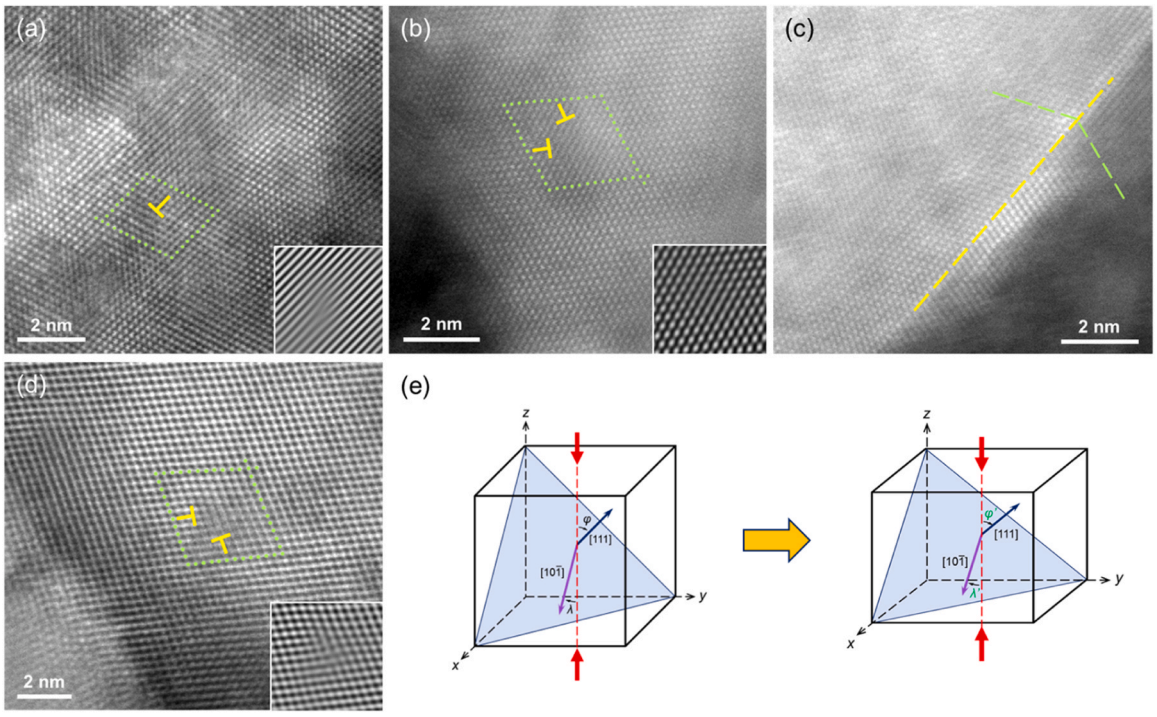

Fig. 4. (a)–(d): HRTEM images showing the representative microstructures observed in the samples recovered from non-hydrostatic compressions. (a) dislocation in 200 nm Ni, (b) dislocation in 20 nm Ni, (c) twin in 20 nm Ni and (d) dislocation in 40 nm CeO_2. Insets: inverse fast Fourier transform results of the areas with dislocations. (e) Schematic diagram to illustrate the effect of anisotropic lattice strain on the Schmid factor of the {111}<1$\bar{1}$0> slip in Ni. The deformation of the unit cell is exaggerated for better illustration.

from ~0.408 to ~0.394 as the differential lattice aspect ratio *r* increases from 0% to 3%. This mutual enhancement mechanism regarding the variation of Schmid factor provides an alternative interpretation of the high-pressure strengthening in nanograined materials [13]. Furthermore, the changeable Schmid factor induced by lattice strain anisotropy might enable us to selectively control the dislocation activity, thereby enhancing plasticity and toughness in inherently brittle materials.

4. Conclusion

We developed an analytical paradigm to estimate the differential lattice aspect ratio of specifically oriented grains in DAC, and systematically investigated the lattice strain anisotropy of nickel and ceria across varying grain sizes under non-hydrostatic compression. We found that the capacity to sustain anisotropic lattice strain is strongly dictated by bond type and grain size. Specifically, the metal has limited lattice strain anisotropy under differential stress, but this limit increases significantly with the decrease of the grain size down to nanometer-scale. On the other hand, the ceramic demonstrates a robust, continuous increase in lattice strain anisotropy with rising stress, while the enhancement gained from grain size reduction is less pronounced. Both materials exhibit large maximum lattice anisotropy (up to ~3.2% for {200} planes) as the grain sizes are reduced to ~8 nm, highlighting their broad parameter spaces under non-hydrostatic compression. Supported by microstructural evidence, we conclude that this size-dependency primarily originates from the respective inhibition and activation of plastic slip in nanograined metals and ceramics. The strengthening mechanism of compressed nanograined metals from the perspective of lattice strain anisotropy has been discussed. Our work reveals the intrinsic evolution of elastic-plastic deformation in two fundamental material systems, and establishes a foundational reference to the realization of effective property modification via high-pressure strain engineering.

CRediT authorship contribution statement

Xiaoling Zhou: Writing – review & editing, Supervision, Resources, Funding acquisition, Data curation. **Haini Dong:** Methodology, Investigation, Data curation. **Bin Chen:** Writing – review & editing, Supervision, Resources, Funding acquisition, Conceptualization. **Jianing Xu:** Methodology, Investigation, Data curation. **Mingzhi Yuan:** Writing – review & editing, Writing – original draft, Visualization, Methodology, Investigation, Formal analysis, Conceptualization.

Declaration of Competing Interest

The authors declare that they have no known competing financial interests or personal relationships that could have appeared to influence the work reported in this paper.

Acknowledgements

We thank Dr. Jinyuan Yan for the support in synchrotron experiments and Dr. Zifan Wang for the helpful discussions. This work is supported by the National Natural Science Foundation of China (12202126, 12274101) and Shenzhen Startup Fund for Talents. X. Z. acknowledges the support of the Talent Recruitment Project of Guangdong (No. 2021QN02C100). This research used the resources of the Advanced Light Source, which is a DOE Office of Science User Facility under contract number DE-AC02–05CH11231. This research was partially supported by COMPRES, the Consortium for Materials Properties Research in Earth Sciences under NSF Cooperative Agreement EAR 1606856.

Appendix A. Supporting information

Supplementary data associated with this article can be found in the online version at doi:10.1016/j.mtcomm.2026.115100.

Data availability

Data will be made available on request.

References

[1] V.M. Pereira, A.H. Castro Neto, Strain engineering of graphene's electronic structure, Phys. Rev. Lett. 103 (2009) 046801, https://doi.org/10.1103/PhysRevLett.103.046801.

[2] Z. Dai, L. Liu, Z. Zhang, Strain engineering of 2D materials: issues and opportunities at the interface, Adv. Mater. 31 (2019) 1805417, https://doi.org/10.1002/adma.201805417.

[3] C. Dang, J.-P. Chou, B. Dai, C.-T. Chou, Y. Yang, R. Fan, W. Lin, F. Meng, A. Hu, J. Zhu, J. Han, A.M. Minor, J. Li, Y. Lu, Achieving large uniform tensile elasticity in microfabricated diamond, Science 371 (2021) 76–78, https://doi.org/10.1126/science.abc4174.

[4] Y. Chen, Y. Lei, Y. Li, Y. Yu, J. Cai, M.-H. Chiu, R. Rao, Y. Gu, C. Wang, W. Choi, H. Hu, C. Wang, Y. Li, J. Song, J. Zhang, B. Qi, M. Lin, Z. Zhang, A.E. Islam, B. Maruyama, S. Dayeh, L.-J. Li, K. Yang, Y.-H. Lo, S. Xu, Strain engineering and epitaxial stabilization of halide perovskites, Nature 577 (2020) 209–215, https://doi.org/10.1038/s41586-019-1868-x.

[5] Z. Xia, S. Guo, Strain engineering of metal-based nanomaterials for energy electrocatalysis, Chem. Soc. Rev. 48 (2019) 3265–3278, https://doi.org/10.1039/C8CS00846A.

[6] S. Hao, L. Cui, D. Jiang, X. Han, Y. Ren, J. Jiang, Y. Liu, Z. Liu, S. Mao, Y. Wang, Y. Li, X. Ren, X. Ding, S. Wang, C. Yu, X. Shi, M. Du, F. Yang, Y. Zheng, Z. Zhang, X. Li, D.E. Brown, J. Li, A transforming metal nanocomposite with large elastic strain, low modulus, and high strength, Science 339 (2013) 1191–1194, https://doi.org/10.1126/science.1228602.

[7] J. Li, Z. Shan, E. Ma, Elastic strain engineering for unprecedented materials properties, MRS Bull. 39 (2014) 108–114, https://doi.org/10.1557/mrs.2014.3.

[8] H.-K. Mao, X.-J. Chen, Y. Ding, B. Li, L. Wang, Solids, liquids, and gases under high pressure, Rev. Mod. Phys. 90 (2018) 015007, https://doi.org/10.1103/RevModPhys.90.015007.

[9] H.-K. Mao, B. Chen, J. Chen, K. Li, J.-F. Lin, W. Yang, H. Zheng, Recent advances in high-pressure science and technology, Matter Radiat. Extrem. 1 (2016) 59–75, https://doi.org/10.1016/j.mre.2016.01.005.

[10] A.K. Singh, C. Balasingh, H.-k Mao, R.J. Hemley, J. Shu, Analysis of lattice strains measured under nonhydrostatic pressure, J. Appl. Phys. 83 (1998) 7567, https://doi.org/10.1063/1.367872.

[11] S. Merkel, A. Kubo, L. Miyagi, S. Speziale, T. Duffy, H.-k Mao, H.-R. Wenk, Plastic deformation of $MgGeO_3$ post-perovskite at lower mantle pressures, Science 311 (2006) 644–646, https://doi.org/10.1126/science.1121808.

[12] B. Chen, K. Lutker, S.V. Raju, J. Yan, W. Kanitpanyacharoen, J. Lei, S. Yang, H.-R. Wenk, H.-k Mao, Q. Williams, Texture of nanocrystalline nickel: probing the lower size limit of dislocation activity, Science 338 (2012) 1448–1451, https://doi.org/10.1126/science.1228211.

[13] X. Zhou, Z. Feng, L. Zhu, J. Xu, L. Miyagi, H. Dong, H. Sheng, Y. Wang, Q. Li, Y. Ma, H. Zhang, J. Yan, N. Tamura, M. Kunz, K. Lutker, T. Huang, D.A. Hughes, X. Huang, B. Chen, High-pressure strengthening in ultrafine-grained metals, Nature 579 (2020) 67–72, https://doi.org/10.1038/s41586-020-2036-z.

[14] J. Hu, Y.N. Shi, X. Sauvage, G. Sha, K. Lu, Grain boundary stability governs hardening and softening in extremely fine nanograined metals, Science 355 (2017) 1292–1296, https://doi.org/10.1126/science.aal5166.

[15] I.A. Ovid'ko, R.Z. Valiev, Y.T. Zhu, Review on superior strength and enhanced ductility of metallic nanomaterials, Prog. Mater. Sci. 94 (2018) 462–540, https://doi.org/10.1016/j.pmatsci.2018.02.002.

[16] B. Gilbert, F. Huang, H. Zhang, G.A. Waychunas, J.F. Banfield, Nanoparticles: strained and stiff, Science 305 (2004) 651–654, https://doi.org/10.1126/science.1098454.

[17] E.O. Hall, The deformation and ageing of mild steel: III discussion of results, Proc. Phys. Soc. Lond. B 64 (1951) 747–753, https://doi.org/10.1088/0370-1301/64/9/303.

[18] N.J. Petch, The cleavage strength of polycrystals, J. Iron Steel Inst. 174 (1953) 25–28.

[19] Y. Fei, A. Ricolleau, M. Frank, K. Mibe, G. Shen, V. Prakapenka, Toward an internally consistent pressure scale, Proc. Natl. Acad. Sci. USA 104 (2007) 9182–9186, https://doi.org/10.1073/pnas.0609013104.

[20] A.P. Hammersley, FIT2D: an introduction and overview. ESRF Internal Report ESRF97HA02T, 1997.

[21] S. Merkel, N. Hilairet, Multifit/Polydefix: a framework for the analysis of polycrystal deformation using X-rays, J. Appl. Cryst. 48 (2015) 1307–1313, https://doi.org/10.1107/S1600576715010390.

[22] Y. Wang, F. Shi, J. Gasc, H. Ohfuji, B. Wen, T. Yu, T. Officer, N. Nishiyama, T. Shinmei, T. Irifune, Plastic deformation and strengthening mechanisms of nanopolycrystalline diamond, ACS Nano 15 (2021) 8283–8294, https://doi.org/10.1021/acsnano.0c08737.

[23] M. Dao, L. Lu, R.J. Asaro, J.T.M. De Hosson, E. Ma, Toward a quantitative understanding of mechanical behavior of nanocrystalline metals, Acta Mater. 55 (2007) 4041–4065, https://doi.org/10.1016/j.actamat.2007.01.038.

[24] H. Li, H. Choo, Y. Ren, T.A. Saleh, U. Lienert, P.K. Liaw, F. Ebrahimi, Strain-dependent deformation behavior in nanocrystalline metals, Phys. Rev. Lett. 101 (2008) 015502, https://doi.org/10.1103/PhysRevLett.101.015502.

[25] J. Xu, T. Huang, H. Dong, D. Tan, Z. Feng, T. Wei, R.A. Susilo, Y. Wang, H. Wang, M. Yuan, L. Zhang, S. Wan, Y. Huang, T. Lu, Y. Chen, Z. Chen, B. Chen, Structural and mechanical properties of magnesium aluminate nanoceramics under high pressure, Appl. Phys. Lett. 117 (2020) 041901, https://doi.org/10.1063/5.0010180.

[26] H. Wang, M. Yuan, H. Li, B. Chen, The mechanical properties of nanoceramic CeO_2 under high pressure, MRS Commun. 13 (2023) 1125–1130, https://doi.org/10.1557/s43579-023-00401-x.

[27] G.W. Groves, A. Kelly, Independent slip systems in crystals, Philos. Mag. 8 (1963) 877–887, https://doi.org/10.1080/14786436308213843.

[28] M. Chen, E. Ma, K.J. Hemker, H. Sheng, Y. Wang, X. Cheng, Deformation twinning in nanocrystalline aluminum, Science 300 (2003) 1275–1277, https://doi.org/10.1126/science.1083727.

[29] B. Chen, K. Lutker, J. Lei, J. Yan, S. Yang, H.-k Mao, Detecting grain rotation at the nanoscale, Proc. Natl. Acad. Sci. USA 111 (2014) 3350–3353, https://doi.org/10.1073/pnas.1324184111.

[30] Q. He, S. Schmidt, W. Zhu, G. Wu, T. Huang, L. Zhang, D.J. Jensen, Z. Feng, A. Godfrey, X. Huang, 3D microscopy at the nanoscale reveals unexpected lattice rotations in deformed nickel, Science 382 (2023) 1065–1069, https://doi.org/10.1126/science.adj2522.

[31] Z. Shan, E.A. Stach, J.M.K. Wiezorek, J.A. Knapp, D.M. Follstaedt, S.X. Mao, Grain boundary-mediated plasticity in nanocrystalline nickel, Science 305 (2004) 654–657, https://doi.org/10.1126/science.1098741.

[32] J. Schiøtz, K.W. Jacobsen, A maximum in the strength of nanocrystalline copper, Science 301 (2003) 1357–1359, https://doi.org/10.1126/science.1086636.

[33] A.A. Tsirlin, B.R. Ortiz, M. Dressel, S.D. Wilson, S. Winnerl, E. Uykur, Effect of nonhydrostatic pressure on the superconducting kagome metal CsV_3Sb_5, Phys. Rev. B 107 (2023) 174107, https://doi.org/10.1103/PhysRevB.107.174107.

[34] S. Duwal, C.-S. Yoo, Shear-induced isostructural phase transition and metallization of layered tungsten disulfide under nonhydrostatic compression, J. Phys. Chem. C 120 (2016) 5101–5107, https://doi.org/10.1021/acs.jpcc.5b10759.

[35] W. Yu, A.A. Aczel, T.J. Williams, S.L. Bud'ko, N. Ni, P.C. Canfield, G.M. Luke, Absence of superconductivity in single-phase $CaFe_2As_2$ under hydrostatic pressure, Phys. Rev. B 79 (2009) 020511, https://doi.org/10.1103/PhysRevB.79.020511.